

# Thermonuclear reactions probed at stellar-core conditions with laser-based inertial-confinement fusion

D. T. Casey<sup>1\*</sup>, D. B. Sayre<sup>1</sup>, C. R. Brune<sup>2</sup>, V. A. Smalyuk<sup>1</sup>, C. R. Weber<sup>1</sup>, R. E. Tipton<sup>1</sup>, J. E. Pino<sup>1</sup>, G. P. Grim<sup>1</sup>, B. A. Remington<sup>1</sup>, D. Dearborn<sup>1</sup>, L. R. Benedetti<sup>1</sup>, J. A. Frenje<sup>3</sup>, M. Gatu-Johnson<sup>3</sup>, R. Hatarik<sup>1</sup>, N. Izumi<sup>1</sup>, J. M. McNaney<sup>1</sup>, T. Ma<sup>1</sup>, G. A. Kyrala<sup>4</sup>, S. MacLaren<sup>1</sup>, J. Salmonson<sup>1</sup>, S. F. Khan<sup>1</sup>, A. Pak<sup>1</sup>, L. Berzak Hopkins<sup>1</sup>, S. LePape<sup>1</sup>, B. K. Spears<sup>1</sup>, N. B. Meezan<sup>1</sup>, L. Divol<sup>1</sup>, C. B. Yeamans<sup>1</sup>, J. A. Caggiano<sup>1</sup>, D. P. McNabb<sup>1</sup>, D. M. Holunga<sup>1</sup>, M. Chiarappa-Zucca<sup>1</sup>, T. R. Kohut<sup>1</sup> and T. G. Parham<sup>1</sup>

**Stars are giant thermonuclear plasma furnaces that slowly fuse the lighter elements in the universe into heavier elements, releasing energy, and generating the pressure required to prevent collapse. To understand stars, we must rely on nuclear reaction rate data obtained, up to now, under conditions very different from those of stellar cores. Here we show thermonuclear measurements of the  ${}^2\text{H}(\text{d},\text{n}){}^3\text{He}$  and  ${}^3\text{H}(\text{t},2\text{n}){}^4\text{He}$  S-factors at a range of densities ( $1.2\text{--}16\text{ g cm}^{-3}$ ) and temperatures ( $2.1\text{--}5.4\text{ keV}$ ) that allow us to test the conditions of the hydrogen-burning phase of main-sequence stars. The relevant conditions are created using inertial-confinement fusion implosions at the National Ignition Facility. Our data agree within uncertainty with previous accelerator-based measurements and establish this approach for future experiments to measure other reactions and to test plasma-nuclear effects present in stellar interiors, such as plasma electron screening, directly in the environments where they occur.**

Computational models<sup>1,2</sup> that require accurate nuclear reaction rate measurements are needed to both understand stellar objects and predict how they will evolve. Accelerator-based experiments that generally make these nuclear reaction rate measurements are particularly challenging at the low centre-of-mass energies ( $E_{\text{cm}} \sim 10\text{--}30\text{ keV}$ ) relevant to stellar nucleosynthesis, as the reaction cross-sections fall rapidly with decreasing energy, bound electron screening corrections become significant, and terrestrial and cosmic background sources become a major experimental challenge<sup>3–5</sup>. Moreover, experiments are often extrapolated to stellar relevant energies from higher energy where the measurements are more straightforward. That extrapolation is made easier when the strong energy-dependent aspects of the cross-section (de Broglie wavelength and the Coulomb barrier) are removed by recasting the cross-section in terms of the S-factor<sup>2</sup>. The  ${}^3\text{He}({}^3\text{He},2\text{p}){}^4\text{He}$  (or  ${}^3\text{he}^3\text{he}$  for short) reaction, which is important in stellar burning of hydrogen, is one of the only cases where measurements have reached energies in the solar reactant energy window<sup>3,4,6</sup>. In most cases, the extrapolations that are required could result in significant error if an unexpected resonance exists. In fact, before measurements were available, an unknown resonance for  ${}^3\text{he}^3\text{he}$  was once proposed<sup>7</sup> as a possible explanation for the ‘solar neutrino problem’, later explained instead using neutrino oscillations<sup>8–10</sup>. Theoretical work<sup>11</sup> argued against such a  ${}^3\text{he}^3\text{he}$  low-energy resonance because it was not predicted or observed in the mirror  ${}^3\text{H}(\text{t},2\text{n}){}^4\text{He}$  reaction. Measuring these S-factors directly at the relevant hot, dense, thermonuclear plasma conditions would avoid these issues with

backgrounds, screening corrections, and extrapolations, but this was long thought to be impractical or impossible for any reaction. Here, we present the first thermonuclear measurements of the S-factors for the  ${}^2\text{H}(\text{d},\text{n}){}^3\text{He}$  (or dd) and  ${}^3\text{H}(\text{t},2\text{n}){}^4\text{He}$  (or tt) reactions enabled by new experimental capabilities developed at the National Ignition Facility (NIF)<sup>12</sup>. Although these reactions do not themselves occur appreciably in the hydrogen-burning cores of stars, they are important for other astrophysical reasons outlined below. Furthermore, this work helps demonstrate a capability to perform nuclear measurements at densities and temperatures relevant for testing stellar-core conditions.

The tt reaction has been determined in our experiments at the lowest reactant energy reported to date, which has particular nuclear-astrophysical interest through the mirror relationship to  ${}^3\text{he}^3\text{he}$ . Both the dd and tt measurements show good agreement with up-to-date nuclear databases. This supports earlier theoretical conclusions<sup>11</sup> and the direct measurements of  ${}^3\text{he}^3\text{he}$  that have been performed using the LUNA accelerator facility<sup>3,4</sup> that showed no resonant behaviour in the solar reactant energy window. The  ${}^3\text{he}^3\text{he}$  reaction is also of interest in explaining the low cosmic abundance of  ${}^3\text{He}$  by destruction in post-main sequence, red giant stars. These stars have a deep mixing mechanism from the hydrogen-burning shell to the base of the convective envelope seeded by the small change in the mean molecular weight resulting from this reaction<sup>13</sup> that results in enhanced  ${}^3\text{he}^3\text{he}$  burning and thus lowering the  ${}^3\text{He}$  cosmic abundance. The burning of deuterium, mainly through  ${}^2\text{H}(\text{p},\gamma){}^3\text{He}$  and to a lesser extent dd, is interesting as it can

<sup>1</sup>Lawrence Livermore National Laboratory, Livermore, California 94550, USA. <sup>2</sup>Ohio University, Athens, Ohio 45701, USA. <sup>3</sup>Massachusetts Institute of Technology, Cambridge, Massachusetts 02139, USA. <sup>4</sup>Los Alamos National Laboratory, Los Alamos, New Mexico 87545, USA. \*e-mail: [casey21@llnl.gov](mailto:casey21@llnl.gov)

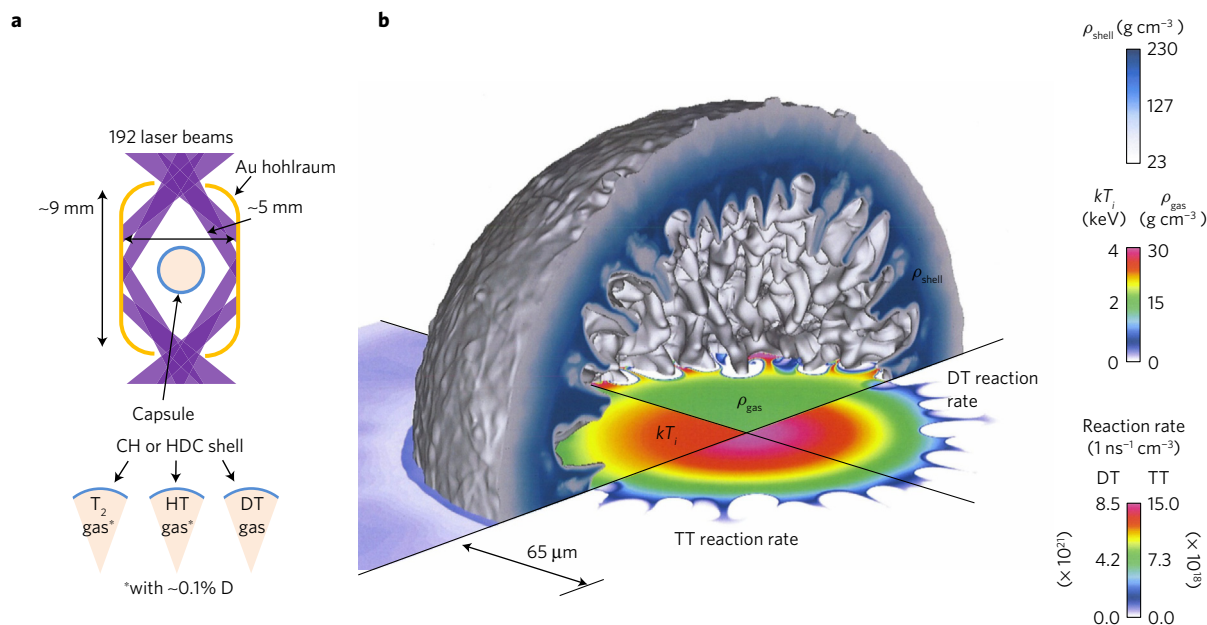


**Figure 1 | Experimental setup and conditions achieved at peak burn.** **a**, Illustration of the experimental configuration. A gold cylindrical cavity (hohlraum) surrounds a capsule filled with either  $T_2$  or HT gas (with  $\sim 0.1$  atom-% D) or nearly 50% D and 50% T. The laser energy of 0.8–1.5 MJ is delivered by 192 laser beams into a hollow Au hohlraum producing thermal X-rays that ablatively compress and heat the gas inside the capsule to stellar-like conditions. **b**, A 3D MIRANDA simulation<sup>17</sup> of the capsule implosion at peak nuclear reaction rate showing the density of the plastic shell, density of the gas, temperature of the gas, and predicted reaction rate for dt and tt reactions using evaluated reactivities. On the right-hand side, the colour bars show the density, temperature, and the reaction rate, where  $1 \text{ ns}^{-1} \text{ cm}^{-3}$  is reactions per nanosecond per  $\text{cm}^3$  of volume.

impact the formation of stars by slowing or stalling the collapse of a molecular gas cloud or proto-star<sup>14</sup>. Deuterium burning is similarly interesting for brown-dwarf stars ( $>13$  times the mass of Jupiter), which are stars that do not have enough mass to eventually burn hydrogen after deuterium depletion<sup>15</sup>. The dd reaction is also important for Big Bang Nucleosynthesis (BBN) in the production of  $^3\text{He}$  and the measurements reported here sample the low-energy (and therefore most challenging) end of the relevant energy range 10 keV–2.5 MeV (ref. 16).

The measurements reported here were conducted using inertial-confinement fusion (ICF) experiments at the NIF that produced, at the time of nuclear burn, imploded core conditions equivalent to the temperatures and densities found in stellar cores (shown later in Fig. 2). In these experiments, fuel-(gas)-filled capsules are compressed to temperatures and densities where significant fusion reactions occur. A sketch of the experimental configuration is provided in Fig. 1a. The 192 NIF laser beams irradiate the inside of a cylindrical Au cylinder (or hohlraum) with 0.8–1.5 MJ of energy, delivered over tens of nanoseconds. This produces quasi-thermal X-rays that subsequently ablate the outer portion of a hollow plastic or high-density carbon capsule (details can be found in the Supplementary Extended Data section). This ablation sends the remaining capsule material imploding inwards, compressing and heating a gas cavity filled with either tritium ( $T_2$ ) or hydrogen–tritium mixture (HT) with a small amount of deuterium (D), or a nearly equimolar DT gas. The resulting implosion produces a hot, dense plasma core, where nuclear reactions occur, that are observed using neutron and X-ray diagnostics.

To illustrate these conditions, Fig. 1b shows the results of a three-dimensional (3D) simulated implosion at the time of peak compression and burn using the hydrodynamics code MIRANDA<sup>17</sup>. This simulation was initialized during the linear stage<sup>18</sup> of hydrodynamic instability growth from a radiation hydrodynamics calculation using HYDRA<sup>19</sup> and measured capsule perturbations. Figure 1b shows the density of the plastic shell in the upper region, and the density and temperature of the nuclear fuel projected

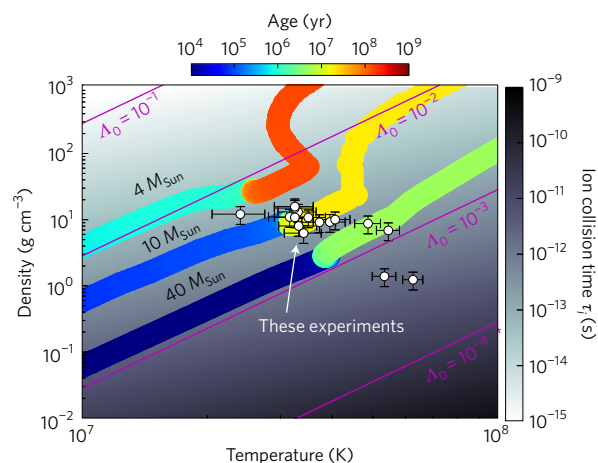


**Figure 2 | Comparison of the core conditions of several stellar systems to those achieved in the experiments described herein.** Stellar-core density (left-hand vertical axis) and temperature trajectory (horizontal axis) versus time (curves with colour scale) for  $4 M_{\text{Sun}}$ ,  $10 M_{\text{Sun}}$ , and  $40 M_{\text{Sun}}$  mass stars during their evolution. The background grey scale is the ion–ion collision time along with the charge-independent plasma parameter (purple contours). Also included (open symbols with error bars) are experimentally inferred burn-averaged temperatures and densities for the ICF experiments discussed herein.

below, as well as the tt and  $^3\text{H}(\text{d},\text{n})^4\text{He}$  (or dt) reaction rates in the lowest quadrants. By the time shown, the shell of the capsule develops nonlinear spikes and bubbles due to the Rayleigh–Taylor instability, setting up a complex flow field near the shell–gas interface<sup>20,21</sup>. The inward protruding shell perturbations have impacted the formation of the outer core, resulting in complicated density and temperature profiles. The evaluated nuclear data file (ENDF/B-VII.1) reactivities<sup>22</sup> were used to compute the dd, dt, and tt reaction rates (only dt and tt are shown), which show

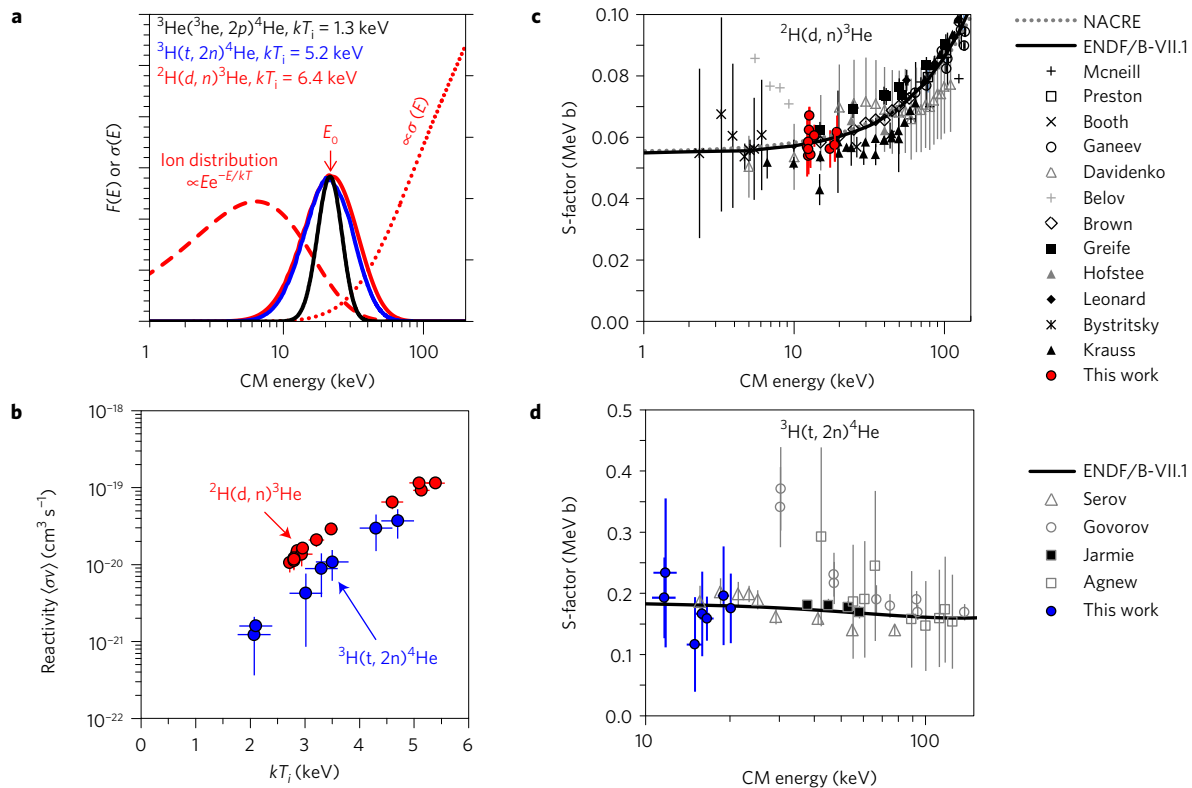


**Figure 3 | Thermonuclear reactivity and S-factor data for  ${}^2\text{H}(\text{d}, \text{n}){}^3\text{He}$  and  ${}^3\text{H}(\text{t}, 2\text{n}){}^4\text{He}$ .** **a**, Plot of  ${}^2\text{H}(\text{d}, \text{n}){}^3\text{He}$  cross-section (dotted red curve), centre-of-mass energy distribution at  $kT_i = 6.4$  keV (dashed red curve), and resultant reactant energy distribution (solid red curve). Also shown are the  ${}^3\text{H}(\text{t}, 2\text{n}){}^4\text{He}$  (solid blue curve) and  ${}^3\text{He}({}^3\text{He}, 2\text{p}){}^4\text{He}$  (solid black curve) reactant distributions with the same  $E_0$ . **b**, Measured reactivity for the  ${}^2\text{H}(\text{d}, \text{n}){}^3\text{He}$  and  ${}^3\text{H}(\text{t}, 2\text{n}){}^4\text{He}$  reactions as a function of the measured temperature. **c**, Inferred S-factor for the  ${}^2\text{H}(\text{d}, \text{n}){}^3\text{He}$  reaction. **d**, Inferred S-factor for the  ${}^3\text{H}(\text{t}, 2\text{n}){}^4\text{He}$  reaction. Included also are comparisons to data from accelerator experiments<sup>29–44</sup> and the NACRE<sup>26</sup> and ENDF/B-VII.1 (refs 22, 45) evaluations.

evolving profiles in the presence of strong temperature and density gradients. It is shown in the Methods that the effects of these gradients are insignificant when studying reactivity ratios measured simultaneously from the same experiment. It is also shown that this technique is robust to complex temporally and spatially evolving burn profiles, independent of complicated models or simulations.

To illustrate the conditions of some relevant stellar systems for comparison, Fig. 2 shows the simulated temperature and density trajectory of stellar cores for stars with 4, 10, and 40 solar masses ( $M_{\text{sun}}$ ), with the colour of the curves representing the age of the star at that point in its evolution. This stellar density and temperature behaviour can be understood using a hydrostatic equilibrium model balancing the gravitational force and the pressure ( $P$ ) via  $dP/dr = -Gm(r)\rho(r)/r^2$ , where  $r$  is the radial spatial coordinate,  $m(r)$  is the mass integrated up to  $r$ ,  $\rho$  is the density, and  $G$  is the gravitational constant. By integrating this expression and assuming a given polytropic-index equation of state, the central core temperature ( $T_c$ ) and density ( $\rho_c$ ) can be shown<sup>2</sup> to be roughly related like  $kT_c \propto M^{2/3} \rho_c^{1/3}$ , where  $M$  is the total mass of the star, and  $k$  is the Boltzmann constant. Therefore, the larger mass stars generally burn hotter, faster (due to the strong temperature dependence of the reaction rates), and at lower density at equivalent stages of life (for example, the main sequence). The pp cycle dominates hydrogen burning in stars below  $kT_i < 2 \times 10^7$  K, whereas for more massive stars like those in Fig. 2, the carbon–nitrogen–oxygen (CNO) cycle dominates<sup>23</sup>. The hydrogen-burning phase or main sequence occurs on each curve where these stars spend most of their lives or where the colour scale representing the age of the star in years makes the most abrupt change (although each star continues to evolve for a short while beyond the boundary of the plot).

Also included on Fig. 2 are the ICF experiments discussed in this study with the measured burn-averaged density and temperature from the implosions, which were determined directly from the data. The Doppler broadening of the dt neutron peak provides a burn-averaged ion temperature, while the yield combined with the X-ray core volume and X-ray emission time history can be used to estimate the core pressure (since peak burn is expected to occur near peak compression and X-ray emission) and assuming an ideal equation of state, the core density<sup>24</sup>. Figure 2 also shows contours of the charge-independent plasma parameter ( $\Lambda_0 = (4\pi)^{1/2} e^3 n^{1/2} / (kT)^{3/2}$ ) from which the plasma parameter ( $\Lambda = U/kT$ ), defined as the Coulomb potential energy ( $U$ ) over the thermal kinetic energy ( $kT$ ), follows as  $\Lambda = Z_1 Z_2 \tilde{z} \Lambda_0$  (ref. 5). Here  $Z_1$  and  $Z_2$  are the atomic numbers of the reacting nuclei,  $\tilde{z}$  is the atomic number of the background plasma, and  $n$  is the total ion density (note that a factor of  $(kT)^{-1/2}$  comes from the Debye radius in estimating  $U$ ). Interestingly, the impact of plasma screening on the ICF implosion experiments can be estimated directly using  $\Lambda$  to have enhanced the cross-section by only  $\sim 0.05$ – $0.5\%$  (described in more detail in the Methods). This weak plasma screening provides the opportunity to study these bare-nucleus S-factors at very low energy in the absence of bound electron screening corrections. Furthermore, this platform may provide an opportunity to test plasma screening itself, if  $\Lambda$  can be increased in future experiments.

The background grey scale shows the ion–ion collision time  $\tau_i$  (normalized so that for non-DT plasmas one should multiply by  $Z^{-4} \sqrt{\mu/2.5}$ , where  $\mu$  is the mass in amu)<sup>25</sup>. During the main sequence, these stars are held in hydrostatic equilibrium for  $\sim 1 \times 10^{14}$ – $5 \times 10^{15}$  s by a balance between the gravitational force and internal pressure until an appreciable amount of the



fuel maintaining that equilibrium is depleted. In contrast, these ICF implosions are held by the inertia of the assembled shell for  $t \sim \sqrt{\rho \Delta R / P}$ , where  $\rho \Delta$  is the shell areal density,  $R$  is the core radius, and  $P$  is the core pressure, which equates to burn widths (which are somewhat shorter due to the strong temperature weighting of the burn) of  $\sim 2 \times 10^{-10}$ – $3.5 \times 10^{-10}$  s. Despite the enormous difference in scale, the implosion cores take on thermonuclear conditions much like those of stellar cores, as they are held together for sufficient time such that each ion undergoes  $\sim 10^3$ – $10^5$  collisions over the course of the burn.

The reactivity  $\langle \sigma v \rangle$  describes the probability of two reactants undergoing a fusion reaction in a thermonuclear plasma and is determined by integrating the cross-section ( $\sigma$ ) times the relative velocity ( $v$ ) over the Maxwellian energy distribution, indicated graphically in Fig. 3a. Figure 3b shows the dd and tt reactivities determined from the measured yield ratios  $Y_{dd}/Y_{dt}$  and  $Y_{tt}/Y_{dt}$  (procedure is outlined in the Methods). These two data sets (dd and tt) span core ion temperatures from 2.5–5.5 keV for dd and 2.0–5.0 keV for tt. These conditions were controlled by changing the target design, drive laser energy, and power used (see details in the Supplementary Extended Data section).

Figure 3c,d show the S-factors using for the dd and tt reactions (procedure outlined in the Methods). For comparison to accelerator measurements, the energy of the peak of the reactant energy distribution  $E_0$  is used as the CM energy abscissa for the ICF implosions. The horizontal error bar is the estimated uncertainty in  $E_0$ . The vertical error bars incorporate both statistical and estimated systematic uncertainties due to initial d and t fuel fractions and measured temperatures (the sensitivity to the temperature uncertainty is weaker than it may seem because of a partial cancellation of the temperature-dependent terms in the yield ratio) and are generally comparable with those from accelerator experiments at these low energies. The results (red and blue symbols) show good agreement with the ENDF/B-VII.1 evaluation (solid curve)<sup>22</sup> for both reactions and the NACRE evaluation for dd (dotted curve)<sup>26</sup>. It is also worth pointing out that the measurements in Fig. 3d at 12 keV are at lower energy than previously reported.

These experiments demonstrate a new experimental capability to produce and diagnose high-energy-density plasmas relevant to nuclear astrophysics. We have shown that the densities and temperatures relevant to stellar interiors can be produced in the laboratory and that nuclear physics experiments can be performed in these extreme environments. It is interesting to note that recent experiments also show that the conditions of  $M_{\text{Sun}} = 1$  stars may be accessible in the near future, providing the possibility of recreating the conditions of our Sun's interior in the laboratory. Furthermore, these experiments may provide a path to study plasma-nuclear effects on nuclear cross-sections that are important in stellar models but are only present in the relevant plasma conditions; for example, electron plasma screening. Because plasma screening is relatively weak at these conditions ( $<1\%$ ), such a measurement is challenging. Nevertheless, several experimental design concepts are being explored using deuterated organic gases or high-Z dopants to increase  $\Lambda$  and therefore produce a measurable impact. The experiments reported here, along with recent work to observe nuclear reaction branching ratios<sup>27,28</sup>, bolster confidence in the viability of ICF implosions as a tool to perform nuclear science experiments and help to set the stage for future studies.

## Methods

Methods, including statements of data availability and any associated accession codes and references, are available in the [online version of this paper](#).

Received 1 September 2016; accepted 29 June 2017;  
published online 7 August 2017

## References

- Bethe, H. A. Energy production in stars. *Phys. Rev.* **55**, 434–456 (1939).
- Clayton, D. D. *Principles of Stellar Evolution and Nucleosynthesis: With a New Preface* (University of Chicago Press, 1968).
- Junker, M. *et al.* Cross section of  ${}^3\text{He}({}^3\text{He}, 2p){}^4\text{He}$  measured at solar energies. *Phys. Rev. C* **57**, 2700–2710 (1998).
- Bonetti, R. *et al.* First measurement of the  ${}^3\text{He}({}^3\text{He}, 2p){}^4\text{He}$  cross section down to the lower edge of the solar Gamow peak. *Phys. Rev. Lett.* **82**, 5205–5208 (1999).
- Dzitko, H., Turck-Chieze, S., Delbourgo-Salvador, P. & Lagrange, C. The screened nuclear reaction rates and the solar neutrino puzzle. *Astrophys. J.* **447**, 428–442 (1995).
- Adelberger, E. G. *et al.* Solar fusion cross sections. *Rev. Mod. Phys.* **70**, 1265–1291 (1998).
- Fowler, W. A. What cooks with solar neutrinos? *Nature* **238**, 24–26 (1972).
- Super-Kamiokande, C. *et al.* Evidence for oscillation of atmospheric neutrinos. *Phys. Rev. Lett.* **81**, 1562–1567 (1998).
- Ahmad, Q. R. *et al.* Measurement of the rate of  $\nu_e + d \rightarrow p + p + e^-$  interactions produced by  ${}^8\text{B}$  solar neutrinos at the Sudbury Neutrino Observatory. *Phys. Rev. Lett.* **87**, 071301 (2001).
- Ahmad, Q. R. *et al.* Direct evidence for neutrino flavor transformation from neutral-current interactions in the Sudbury Neutrino Observatory. *Phys. Rev. Lett.* **89**, 011301 (2002).
- Cs   , A. & Langanke, K. Large-space cluster model calculations for the  ${}^3\text{He}({}^3\text{He}, 2p){}^4\text{He}$  and  ${}^3\text{H}({}^3\text{H}, 2n){}^4\text{He}$  reactions. *Nucl. Phys. A* **646**, 387–396 (1999).
- Moses, E. I., Boyd, R. N., Remington, B. A., Keane, C. J. & Al-Ayat, R. The National Ignition Facility: ushering in a new age for high energy density science. *Phys. Plasmas* **16**, 041006 (2009).
- Eggleston, P. P., Dearborn, D. S. P. & Lattanzio, J. C. Deep mixing of  ${}^3\text{He}$ : reconciling Big Bang and stellar nucleosynthesis. *Science* **314**, 1580–1583 (2006).
- Stahler, S. W. Deuterium and the stellar birthline. *Astrophys. J.* **332**, 804–825 (1988).
- Spiegel, D. S., Burrows, A. & Milsom, J. A. The deuterium-burning mass limit for brown dwarfs and giant planets. *Astrophys. J.* **727**, 57 (2011).
- Serpico, P. D. *et al.* Nuclear reaction network for primordial nucleosynthesis: a detailed analysis of rates, uncertainties and light nuclei yields. *J. Cosmol. Astropart. Phys.* **2004**, 010 (2004).
- Cook, A. W. Artificial fluid properties for large-eddy simulation of compressible turbulent mixing. *Phys. Fluids* **19**, 055103 (2007).
- Weber, C. R. *et al.* Three-dimensional hydrodynamics of the deceleration stage in inertial confinement fusion. *Phys. Plasmas* **22**, 032702 (2015).
- Marinak, M. M. *et al.* Three-dimensional HYDRA simulations of National Ignition Facility targets. *Phys. Plasmas* **8**, 2275–2280 (2001).
- Smalyuk, V. A. *et al.* Measurements of an ablator-gas atomic mix in indirectly driven implosions at the National Ignition Facility. *Phys. Rev. Lett.* **112**, 025002 (2014).
- Casey, D. T. *et al.* Development of the CD Symcap platform to study gas-shell mix in implosions at the National Ignition Facility. *Phys. Plasmas* **21**, 092705 (2014).
- Chadwick, M. B. *et al.* ENDF/B-VII.0: next generation evaluated nuclear data library for nuclear science and technology. *Nucl. Data Sheets* **107**, 2931–3060 (2006).
- Adelberger, E. G. *et al.* Solar fusion cross sections. II. The pp chain and CNO cycles. *Rev. Mod. Phys.* **83**, 195–245 (2011).
- Patel, P. *et al.* *Bull. Am. Phys. Soc. 55th Annu. Meeting APS Div. Plasma Phys.* Vol. 58, 16 (American Physical Society, 2013).
- Atzeni, S. & Meyer-ter-Vehn, J. *The Physics of Inertial Fusion* (Oxford Univ. Press, 2004).
- Angulo, C. *et al.* A compilation of charged-particle induced thermonuclear reaction rates. *Nucl. Phys. A* **656**, 3–183 (1999).
- Kim, Y. *et al.* D-T gamma-to-neutron branching ratio determined from inertial confinement fusion plasmas. *Phys. Plasmas* **19**, 056313 (2012).
- Zylstra, A. B. *et al.* Using inertial fusion implosions to measure the T +  ${}^3\text{He}$  fusion cross section at nucleosynthesis-relevant energies. *Phys. Rev. Lett.* **117**, 035002 (2016).
- Data retrieved from the EXFOR database <http://www.nndc.bnl.gov/EXFOR> website on Jul 23, 2015.
- McNeill, K. G. & Keyser, G. M. The relative probabilities and absolute cross sections of the D – D reactions. *Phys. Rev.* **81**, 602–606 (1951).
- Preston, G., Shaw, P. F. D. & Young, S. A. The cross-sections and angular distributions of the D+D reactions between 150 and 450 keV. *Proc. R. Soc. Lond. A* **226**, 206–216 (1954).
- Booth, D. L., Preston, G. & Shaw, P. F. D. The cross section and angular distributions of the D-D reactions between 40 and 90 keV. *Proc. Phys. Soc. A* **69**, 265–270 (1956).
- Ganeev, A. S. *et al.* The D-D reaction in the deuteron energy range 100–1000 keV. *Sov. J. At. Energy* **5**, 21–36 (1958).

34. Davidenko, V. A., Kucher, A. M., Pogrebov, I. S. & Tuturov, I. F. Nuclear reactions in light nuclei. *Sov. J. At. Energy Suppl.* **No 5**, 7 (1957).
35. Belov, A. S., Kusik, V. E. & Ryabov, Yu. V. The nuclear fusion for the reactions  $^2\text{H}(d,n)^3\text{He}$ ,  $^2\text{H}(d,\gamma)^4\text{He}$  at low deuterons energy and cold nuclear fusion. *Il Nuovo Cimento A* **103**, 1647–1650 (1990).
36. Brown, R. E. & Jarmie, N. Differential cross sections at low energies for  $^2\text{H}(d,p)^3\text{H}$  and  $^2\text{H}(d,n)^3\text{He}$ . *Phys. Rev. C* **41**, 1391–1400 (1990).
37. Greife, U., Gorris, F., Junker, M., Rolfs, C. & Zahnow, D. Oppenheimer–Phillips effect and electron screening in d + d fusion reactions. *Z. Phys. A* **351**, 107–112 (1995).
38. Leonard, D. S., Karwowski, H. J., Brune, C. R., Fisher, B. M. & Ludwig, E. J. Precision measurements of  $^2\text{H}(d,p)^3\text{H}$  and  $^2\text{H}(d,n)^3\text{He}$  total cross sections at Big Bang nucleosynthesis energies. *Phys. Rev. C* **73**, 045801 (2006).
39. Bystritsky, V. M. *et al.* Using a Hall accelerator to investigate d(d, n) $^3\text{He}$  and d(p,  $\gamma$ ) $^3\text{He}$  reactions in the astrophysical energy region. *Bull. Russ. Acad. Sci. Phys.* **74**, 531–534 (2010).
40. Serov, V. I., Abramovich, S. N. & Morkin, L. A. Total cross section measurement for the reaction T(t, 2n) $^4\text{He}$ . *At. Energy* **42**, 66–69 (1977).
41. Govorov, A. M., Li, K.-Y., Osetinskii, G. M., Salatskii, V. I. & Sizov, I. V. Total cross section of the T + T reaction in the 60–1140 keV energy range. *Sov. Phys. JETP* **15**, 266–267 (1962).
42. Jarmie, N. & Allen, R. C. T(t,  $\alpha$ )n, n reaction. *Phys. Rev.* **111**, 1121–1128 (1958).
43. Agnew, H. M. *et al.* Measurement of the cross section for the reaction T + T  $\rightarrow$  He $^4$  + 2n + 11.4 Mev. *Phys. Rev.* **84**, 862–863 (1951).
44. Krauss, A., Becker, H. W., Trautvetter, H. P., Rolfs, C. & Brand, K. Low-energy fusion cross sections of D + D and D +  $^3\text{He}$  reactions. *Nucl. Phys. A* **465**, 150–172 (1987).
45. Data retrieved from <http://www.nndc.bnl.gov/ndf> website on Jul 23, 2015.

## Acknowledgements

The authors sincerely thank the NIF operations staff who supported this work. The authors also thank N. Kabadi for discovering an error in equation (9) in an earlier version

of the manuscript. This work was performed under the auspices of the US Department of Energy by Lawrence Livermore National Laboratory under Contract DE-AC52-07NA27344 and by Ohio University under US Department of Energy grant number DE-FG02-88ER40387 and DE-NA0002905.

## Author contributions

D.T.C. shot (experiments) RI (responsible individual), stagnation campaign lead, and nuclear data analysis. D.B.S. nTOF (neutron time of flight) instrument analysis and nuclear data analysis. C.R.B. nuclear data analysis. V.A.S. shot RI and CD symcap campaign lead. C.R.W. three dimensional hydrodynamic simulations. R.E.T. experiment design and one dimensional hydrodynamic simulations. J.E.P. experiment design, CD symcap campaign lead, and two dimensional hydrodynamic simulations. G.P.G. shot RI and nTOF analysis. B.A.R. mix campaign lead. D.D. stellar evolution simulations. L.R.B. shot RI and X-ray image analysis. J.A.F. Magnetic Recoil Spectrometer (MRS) analysis. M.G.-J. MRS analysis. R.H. nTOF analysis. N.I. shot RI and X-ray image analysis. J.M.M. shot RI and nTOF analysis. T.M. shot RI and X-ray image analysis. G.A.K. shot RI and X-ray image analysis. S.M. experiment design and 2shock campaign lead. J.S. experiment design. S.F.K. shot RI and X-ray image analysis. A.P. shot RI and X-ray image analysis. L.B.H. experiment design. S.L. shot RI. B.K.S. experiment design and stagnation campaign lead. N.B.M. experiment design and IDEP campaign lead. L.D. experiment design. C.B.Y. shot RI and activation diagnostics analysis. J.A.C. nTOF analysis. D.P.M. nuclear data analysis. D.M.H. deuterium and tritium operations. M.C.-Z. mass spectrometer data analysis. T.R.K. deuterium and tritium operations. T.G.P. deuterium and tritium operations.

## Additional information

Supplementary information is available in the [online version of the paper](#). Reprints and permissions information is available online at [www.nature.com/reprints](http://www.nature.com/reprints). Publisher's note: Springer Nature remains neutral with regard to jurisdictional claims in published maps and institutional affiliations. Correspondence and requests for materials should be addressed to D.T.C.

## Competing financial interests

The authors declare no competing financial interests.

## Methods

**The S-factor parameterization.** As discussed in the text, fusion reaction cross-sections ( $\sigma$ ) can be expressed in terms of the S-factor<sup>2</sup> ( $S(E)$ ) as

$$\sigma(E) = [S(E)/E]e^{-2\pi\eta(E)} \quad (1)$$

where  $\eta(E) = (1/2\pi)\sqrt{E_G/E}$  is the Sommerfeld parameter. Here  $E_G$  is the Gamow energy<sup>25</sup>, which is  $E_G = 2(\pi\alpha_f Z_1 Z_2)^2 m_r c^2$ , where  $E$  is the centre-of-mass energy,  $Z_1$  and  $Z_2$  are the atomic numbers of the reactant particles,  $m_r$  is the reduced mass,  $\alpha_f$  is the fine structure constant, and  $c$  is the speed of light<sup>2</sup>. This parameterization partly removes the strong energy dependence of the de Broglie wavelength ( $\lambda_B \propto 1/E$ ) of the reactants and the Coulomb barrier penetrability from the fusion cross-section, making extrapolation less complicated. Extrapolation of the S-factor beyond measured data leads to increased uncertainty and the possibility of error due to electron screening (where electrons shield the Coulomb barrier), resonances, or other unknown physics.

**Bound and plasma electron screening.** Screening by bound electrons (sometimes referred to as laboratory screening) is particularly important at low energies (that is, stellar energies) for accelerator-based measurements, requiring model-dependent corrections to obtain S-factors relevant to astrophysical phenomena. A commonly used model<sup>46</sup> is

$$\frac{\sigma_{\text{Screened}}(E)}{\sigma(E)} \approx e^{\pi\eta(E)U_e/E} \quad (2)$$

where  $\sigma_{\text{Screened}}$  is the screened cross-section,  $\sigma$  is the bare-nucleus cross-section,  $E$  is the reactant centre-of-mass energy, and  $U_e$  is the electron-screening energy, which is tabulated and available in Assenbaum and colleagues<sup>46</sup>.

Electron screening of stellar interior plasmas is quite different than that of terrestrial accelerator experiments. This is because for stellar fusion plasmas the cross-section enhancements depend on the plasma properties, such as density and temperature, as the screening of the Coulomb barrier is being done by the surrounding plasma electrons. The experiments discussed in this paper have plasma screening that is similar to that at stellar interior conditions during the early hydrogen-burning phase, which is fairly weak and can be neglected. A commonly used model to estimate the enhancement due to plasma electron screening was developed by Salpeter<sup>47</sup> and is

$$\frac{\sigma_{\text{Screened}}(E)}{\sigma(E)} \approx e^{\Lambda} \quad (3)$$

where  $\Lambda$  defined in the main text. The Salpeter model is expected to be valid only in the case that the screening effects are weak. Other authors<sup>5,48,49</sup> have discussed models of plasma electron screening that may be more appropriate when screening corrections are not weak or electron degeneracy is important.

**Yield ratio method and its insensitivity to  $\rho(\mathbf{r}, t)$  and  $kT(\mathbf{r}, t)$  profiles.** ICF implosions are highly dynamic with varying temporal and spatial profiles, as is clearly evident in Fig. 1b. As a consequence, care must be exercised when inferring thermonuclear reaction rates. To simplify this problem, we utilize the method of yield ratios.

The reaction yield can be expressed as

$$Y_{12} = \int \frac{f_1 f_2}{1 + \delta_{12}} \frac{\rho(\mathbf{r}, t)^2}{\bar{m}^2} \langle \sigma v \rangle_{12} d\mathbf{r} dt \quad (4)$$

where  $f_1$  and  $f_2$  correspond to the reactant atom fractions,  $\bar{m}$  is the average ion mass,  $\rho$  is the density, and  $\delta_{12}$  is the Kronecker delta to prevent double counting of identical reactants, and the integral is over volume and time<sup>25</sup>. Note also that this yield is reaction yield, not neutron yield, which in the case of tt differ by a factor of two because two neutrons are emitted per reaction. The reactivity is

$$\langle \sigma v \rangle_{12} = \int v \sigma(v) f_1(\mathbf{v}_1) f_2(\mathbf{v}_2) d\mathbf{v}_1 d\mathbf{v}_2 \quad (5)$$

which describes the probability of two reactants 1 and 2 undergoing a fusion reaction in a plasma, via the product of the relative velocities of the reacting ions ( $v$ ) and  $\sigma(v)$  integrated over the relative reactant velocity distributions. If we define the reactivity ratio between two identical reactants 11 (for example, dd or tt) and two different reactants 12 (for example, dt) occurring in the same burning plasma as  $R = \langle \sigma v \rangle_{11} / \langle \sigma v \rangle_{12}$ , then assuming  $f_1$  and  $f_2$  are fixed, the yield ratio between reactants of 11 and 12 is

$$\frac{Y_{11}}{Y_{12}} = \frac{1}{2} \frac{f_1}{f_2} \frac{\int \frac{\rho(\mathbf{r}, t)^2}{\bar{m}^2} R \langle \sigma v \rangle_{12} d\mathbf{r} dt}{\int \frac{\rho(\mathbf{r}, t)^2}{\bar{m}^2} \langle \sigma v \rangle_{12} d\mathbf{r} dt} \quad (6)$$

And if

$$\frac{\partial^2 R}{\partial kT^2} \frac{1}{R_0} \sigma_{kT}^2 \ll 1 \quad (7)$$

where  $\sigma_{kT}$  is the variance of the reactant temperature distribution, then we can expand  $R \approx R_0 + (\partial R / \partial kT)(kT - \langle kT \rangle)$ , where  $\langle kT \rangle$  is the fusion-burn-averaged temperature and  $R_0$  is the reactivity ratio evaluated at  $\langle kT \rangle$ . Note that from the S-factor parameterization for the ratio of non-resonant reactions:

$$\frac{\partial^2 R}{\partial kT^2} \approx R_0 \frac{K}{9} \left[ \frac{4}{(kT)^{7/3}} + \frac{K}{(kT)^{8/3}} \right] \quad (8)$$

where the constant  $K$  is

$$K = \frac{-3(\pi\alpha_f)^{2/3} (m_p c^2)^{1/3}}{2^{1/3}} \left[ \left( \frac{Z_1^4 A_1}{2} \right)^{1/3} - \left( \frac{(Z_1 Z_2)^2 A_1 A_2}{A_1 + A_2} \right)^{1/3} \right] \quad (9)$$

Here,  $\alpha_f$  is the fine structure constant,  $A_1$  and  $A_2$  are the atomic mass numbers, and  $m_p c^2$  is the proton rest mass energy. Evaluating  $K$  for the reactions of interest results in  $K = 1.2 \text{ keV}^{1/3}$  for dd/dt and  $K = -1.5 \text{ keV}^{1/3}$  for tt/dt. Simulations of the platforms used in this paper predict the temperature distribution widths are  $\sigma_{kT} = 0.5 \text{ keV}$  at  $\langle kT \rangle = 3.0 \text{ keV}$  and  $\sigma_T = 2.9$  at  $\langle kT \rangle = 5.8 \text{ keV}$  and that the impact of 3D profiles on the temperature width is relatively small (shown in the Supplementary Methods). Direct evaluation confirms that equation (7) is satisfied for both dd/dt and tt/dt, justifying the earlier expansion of  $R$ . Using the  $R$  expansion, the yield ratio becomes

$$\frac{Y_{11}}{Y_{12}} = \frac{1}{2} \frac{f_1}{f_2} R_0 \left[ 1 + \frac{\frac{1}{R_0} \frac{\partial R}{\partial kT} \int \rho(\mathbf{r}, t)^2 (kT - \langle kT \rangle) \langle \sigma v \rangle_{12} d\mathbf{r} dt}{\int \rho(\mathbf{r}, t)^2 \langle \sigma v \rangle_{12} d\mathbf{r} dt} \right] \quad (10)$$

Since

$$\langle kT \rangle = \frac{\int kT \rho(\mathbf{r}, t)^2 \langle \sigma v \rangle_{12} d\mathbf{r} dt}{\int \rho(\mathbf{r}, t)^2 \langle \sigma v \rangle_{12} d\mathbf{r} dt} \quad (11)$$

the second term in the bracket is zero and the yield ratio simplifies to

$$\frac{Y_{11}}{Y_{12}} \approx \frac{1}{2} \frac{f_1}{f_2} \frac{\langle \sigma v \rangle_{11}}{\langle \sigma v \rangle_{12}} \quad (12)$$

Once the reactivity is known, we can arrive at the  $S(E_0)$ , introduced earlier. If  $S(E)$  is slowly varying with energy ( $S'(E_0) \sim 0$  and  $S''(E_0) \sim 0$ ), then the reactivity for a Maxwellian plasma of temperature  $kT$  can be expressed as

$$\langle \sigma v \rangle \approx \sqrt{\frac{2\tau}{m_r kT}} \frac{4}{3} S(E_0) \left( 1 + \frac{5}{12\tau} \right) e^{-\tau} \quad (13)$$

where  $m_r$  is the reduced mass of the reactants,  $\tau = 3E_0/(kT)$ , and  $E_0 = ((kT/2)\sqrt{E_G})^{2/3}$  is the approximate peak for the reactant energy distribution<sup>50</sup>. Solving the above for  $S(E_0)$  and combining with equation (12) gives

$$S(E_0) = \frac{3}{2} \sqrt{\frac{m_r kT}{2\tau}} e^{\tau} \left( 1 + \frac{5}{12\tau} \right)^{-1} \langle \sigma v \rangle_{12} \frac{f_2}{f_1} \frac{Y_{11}}{Y_{12}} \quad (14)$$

The dt yield,  $Y_{12}$ , required in equation (12) is experimentally obtained by measuring the 14 MeV dt neutrons emitted from the implosion. The yield is determined using Cu and Zr activation detectors, the Magnetic Recoil Spectrometer (MRS)<sup>51–54</sup>, and neutron time-of-flight (nTOF) diagnostics<sup>54</sup>. As previously mentioned, the width of the dt neutron peak is used to determine the ion temperature. The dd yield is similarly determined using nTOF detectors (that have been cross-calibrated using In activation and accelerator experiments). Note that the  $^2\text{H}(d,p)^3\text{H}$  also occurs in the DT-filled experiments but the charged-particle products do not escape the dense core and shell assembly, as it exceeds their range. Likewise, the dd and tt reactions also produce charged particles that do not escape at these conditions. Because there are three tt reaction products, the neutron energy spectra extends to zero energy, requiring use of a model to extract the total reaction yield. In this case, the tt reaction yield is determined by measuring the neutron spectrum in the range of 5–10 MeV, using multiple diagnostic techniques<sup>54–56</sup>, then corrected for the neutrons that are outside the 5–10 MeV integral. Recent measurements<sup>57</sup> have improved upon earlier data<sup>58–60</sup> and used a R-matrix model<sup>57,61</sup> that describes the spectrum. By comparing this model to older models, the inferred tt yield differs only by  $\sim 10\%$ , which is assumed to be our error in the total tt yield. This error is much larger than the statistical uncertainty and much smaller than the uncertainty in the initial D concentration. Presently, the model described in ref. 61 is the preferred approach, but improved experimental data for the spectrum at lower energies would be helpful. The emitted neutrons from the dd, tt, and dt reactions are attenuated by the stagnated fuel and capsule material. The level of attenuation depends on the exact implosion platform, but is generally  $< 10\%$  and can be estimated using Monte Carlo simulations.

This approach has been validated using 1D, 2D, and 3D hydrodynamic simulations. For example, the 3D simulation discussed in Fig. 1b using MIRANDA

was used to produce simulated yield and temperature results to test equations (12) and (14), and we find that we are able to recover the simulated reactivities to better than 1% and the corresponding S-factors to better than 2% for both dd and tt reactions, as shown in detail in the Supplementary Information.

**Data availability.** The data that support the plots within this paper and other findings of this study are available in the Supplementary Extended Data online and from the corresponding author upon reasonable request.

## References

46. Assenbaum, H. J., Langanke, K. & Rolfs, C. Effects of electron screening on low-energy fusion cross sections. *Z. Phys. A* **327**, 461–468 (1987).
47. Salpeter, E. E. Electron screening and thermonuclear reactions. *Aust. J. Phys.* **7**, 373–388 (1954).
48. Brown, L. S. & Sawyer, R. F. Nuclear reaction rates in a plasma. *Rev. Mod. Phys.* **69**, 411–436 (1997).
49. Graboske, H. C., Dewitt, H. E., Grossman, A. S. & Cooper, M. S. Screening factors for nuclear reactions. II. Intermediate screening and astrophysical applications. *Astrophys. J.* **181**, 457–474 (1973).
50. Bahcall, J. N. Non-resonant nuclear reactions at stellar temperatures. *Astrophys. J.* **143**, 259–261 (1966).
51. Casey, D. T. *et al.* Measuring the absolute deuterium–tritium neutron yield using the magnetic recoil spectrometer at OMEGA and the NIF. *Rev. Sci. Instrum.* **83**, 10D912 (2012).
52. Cooper, G. W. *et al.* Copper activation deuterium–tritium neutron yield measurements at the National Ignition Facility. *Rev. Sci. Instrum.* **83**, 10D918 (2012).
53. Bleuel, D. L. *et al.* Neutron activation diagnostics at the National Ignition Facility (invited). *Rev. Sci. Instrum.* **83**, 10D313 (2012).
54. Johnson, M. G. *et al.* Neutron spectrometry—an essential tool for diagnosing implosions at the National Ignition Facility (invited). *Rev. Sci. Instrum.* **83**, 10D308 (2012).
55. Yeamans, C. B., Bleuel, D. L. & Bernstein, L. A. Enhanced NIF neutron activation diagnostics. *Rev. Sci. Instrum.* **83**, 10D315 (2012).
56. Frenje, J. A. *et al.* First measurements of the absolute neutron spectrum using the magnetic recoil spectrometer at OMEGA (invited). *Rev. Sci. Instrum.* **79**, 10E502 (2008).
57. Sayre, D. B. *et al.* Measurement of the T+T neutron spectrum using the National Ignition Facility. *Phys. Rev. Lett.* **111**, 052501 (2013).
58. Casey, D. T. *et al.* Measurements of the T(t,2n)<sup>4</sup>He neutron spectrum at low reactant energies from inertial confinement implosions. *Phys. Rev. Lett.* **109**, 025003 (2012).
59. Allen, K. W., Almqvist, E., Dewan, J. T., Pepper, T. P. & Sanders, J. H. The T+T reactions. *Phys. Rev.* **82**, 262–263 (1951).
60. Wong, C., Anderson, J. D. & McClure, J. W. Neutron spectrum from the T+T reaction. *Nucl. Phys.* **71**, 106–112 (1965).
61. Brune, C. R. *et al.* R-matrix description of particle energy spectra produced by low-energy <sup>3</sup>H + <sup>3</sup>H reactions. *Phys. Rev. C* **92**, 014003 (2015).